An Experimental and Modeling Study on Vibro-Acoustic Response of Double-Walled Steel Cylindrical Shells

Xian-Zhong Wang[1,2]·Li Chen[3]·Ning Li[3]·Yu Xia[3] Ye-Ping Xiong[2]

Abstract[*]

Based on precise transfer matrix method (PTMM), the analytical model of the double-walled steel cylindrical shell was setup by taking into account of the annular plate and interlayer water. Under the linear sweep frequency excitation or the fixed frequency excitation, an experimental model of the double-walled steel cylindrical shell has been designed, which is performed to gain the natural frequencies, forced vibration in air and water, underwater acoustic radiation. The analytical model was established to calculate natural frequencies, vibration acceleration level and sound pressure level and compare with the relevant experimental results. The compared results show that analytical results coincide with the experimental value and prove that the analytical model established by PTMM is reliable and credible. Meanwhile, the forced vibration behaviour of measuring positions at inner and outer shells was investigated both theoretically and experimentally. Effects of different types of external excitations on the vibration and sound radiation of the double-walled cylindrical shell are discussed. As to acoustic radiation, the acoustic excitation plays a leading role in the low-frequency range. The force excitation is a major contributor in middle-high frequency range conversely.

Keywords Double-walled cylindrical shells· Sound source excitation· Acoustic radiation· Vibration

1 Introduction

As a general structural configuration, steel cylindrical shells have been widely applied to the design and manufacturing of marine, aerospace and automotive engineering. The excessive dynamic responses of steel cylindrical shells subjected to different loads greatly affect the safety, comfort and health. Due to their superior mechanical and acoustical performance, double-walled steel cylindrical shells are widely applied in Chinese and Russian submarines to realize the insulation and control of vibration and sound radiation. A reliable assessment

Xian-Zhong Wang
xianzhongwang@whut.edu.cn (X. Wang)

[1] Key Laboratory of High Performance Ship Technology (Wuhan University of Technology), Ministry of Education, Wuhan 430063, China
[2] Faculty of Engineering and Physical Sciences, University of Southampton, Southampton, SO17 1BJ, United Kingdom
[3] School of Transportation, Wuhan University of Technology, Wuhan 430063, China

of vibration and sound radiation of double-walled steel cylindrical shells is crucial to guide the structural design and improve the stealth performance. Based on analytical and numerical methods, there is a huge number of works of literature focusing on the dynamic behaviours of cylindrical shells (Mukhopadhyay and Sinha 1992; Ruotolo 2001; Park et al. 2016; Rawat et al. 2019; Temami et al. 2019).

Some analytical methods have been presented for the vibration responses of steel shells, which include Wave analysis method (Li 2009; Gan et al. 2009), Fourier spectral element method (Jin et al. 2017; Su et al. 2016) and Transfer matrix method (Irie et al.1984; Wang et al. 2015). These analytical methods are employed frequently to analyze the dynamic behaviour of single cylindrical shells such as cylindrical shells (Liang et al. 2019; Chen et al 2013), elliptic cylindrical shells (Zhang et al. 2017), ring-stiffened cylindrical shells (Jafari et al. 2006; Wang et al. 2016), but analytical solutions are always limited to considering the existence of the fluid load and ring-stiffeners. There are some semi-analytical methods are also put forward to solve the structure-acoustic problems and investigate other kinds of shell structures like conical-cylindrical shells (Wang et al. 2016b); Qu et al. 2013; Chen et al. 2015) and cylinder-plate combination (Ma et al. 2017; Tso and Hansen 1995). Meyer et al. (2016) derived the condensed transfer functions method to analyze vibration and acoustic radiation of the cylindrical shell with complex interior frame structures. After combining the wave-based method and finite element method, Chen et al. (2018) presented a hybrid analytical technology to study vibration behaviours of the cylindrical shell with interior typical structures. Based on transfer matrix method and precise integration method, Wang et al. (2016a) presented a precise transfer matrix method to solve the vibration response and developed a modified wave superposition method to gain acoustic responses of immersed stiffened combined shells by solving virtual boundary integral equations.

Numerical methods including finite element method (Everstine 1997; De Faria 2004), boundary element method (Ventsel et al. 2010) and coupled finite element and boundary element method (Everstine and Henderson 1990; Liu and Chen 2009) have demonstrated the advantages of computation on solving the dynamic response of complex steel shells. Ettouney et al. (1994) adopted a finite difference method to simulate the shell and analyzed

vibration and acoustic behaviours of the immersed cylindrical shell with an interior beam and two hemispherical end caps. The acoustic-structure interaction problem of complex shells can be solved by the discretization of the domain model and shape functions of the low order, which also restrain the upper limit of frequency range and computational efficiency.

Due to the geometrical and mathematical complexity in constructing the analytical model, there is only some work concerning vibration and acoustic characteristics of double-walled cylindrical shells. Yamada et al. (1986) developed the transfer matrix method to investigate the free vibration of the double-walled cylindrical shell, which is coupled with annular plates at both ends. Bai (2012) employed the modal superposition method to investigate the transmission of sound and vibration performance of submerged double-walled cylindrical shells connected with noncontinuous slab ribs. Combining measuring the vibration of the inner shell, Zhang et al. (2013) presented a modal superposition method to predict the acoustic radiated power of submerged double cylindrical shells. Considering the existence of external mean flow and walls perforated, Zhang et al. (2017) studied the sound transmission loss of a double-walled cylindrical shell subjected to the plane wave.

However, it can be found that only a few articles discussed the experimental investigation and modelling analysis of vibration and sound radiation of immersed double-walled cylindrical shells subjected to force and sound source excitations. Both developing an analytical approximation method and performing an experimental measurement are strongly necessary to investigate the vibration and acoustic behaviours of double-walled cylindrical shells under different excitations. The aim of this study is to provide experimental data of the immersed stiffened double-walled cylindrical shells under force and sound source excitations to fill the data gap. In this study, both linear sweep frequency and fixed frequency were used to carry out the experiments to obtain natural frequencies, vibration acceleration value and sound pressure value under force and acoustic excitations.

Based on the precise transfer matrix method (Wang et al. 2018), the analytical model is improved by taking into consideration of annular plate and interlayer water. Firstly, the field transfer relationship between the inner and outer ends of the annular plate is the first time obtained to construct the interactions between the inner and

outer shells in PTMM. Secondly, interlayer water as the fluid medium generates the radiated noise. Sound pressure acts on the internal surface of the outer shell and outside surface of the inner shell in the form of reaction forces, which should satisfy the Neumann boundary conditions. Then nature frequencies, vibration acceleration level and sound pressure level of the analytical model in vacuo and water are calculated by PTMM and compared with the relevant experimental results, which exhibits its effectiveness and reliability. Particular attention was paid to the effect of the force and sound source excitations on the acoustic radiation of the double-walled cylindrical shell in detail. Meanwhile, The effect of boundary restraints stiffnesses of the double-walled cylindrical shell on the underwater sound radiation is also discussed.

2 Analytical model

The abridge general view of an immersed ring-stiffened double-walled cylindrical shell is shown in Fig.1. The time-dependent function $e^{j\omega t}$ in the below formulas is concealed for convenience and simplicity. The analytical model adopts the same cylindrical coordinates (x, θ, r) to describe the measurement positions.

2.1 The cylindrical shell

Based on the theory of shells, the governing equation of steel cylindrical shell can be expressed as a first-order matrix differential equation form

$$\frac{d\boldsymbol{Z}\left(\xi^i\right)}{d\xi^i}=\mathbf{U}\left(\xi^i\right)\boldsymbol{Z}\left(\xi^i\right)+\boldsymbol{F}\left(\xi^i\right)-\boldsymbol{p}\left(\xi^i\right) \tag{1}$$

where superscripts i=1, 2 represent the inner/outer shell. ξ^i equals x^i/R^i . R^i are the radii of the inner/outer shell. $\boldsymbol{Z}\left(\xi^i\right)=\left\{\tilde{u}^i \quad \tilde{v}^i \quad \tilde{w}^i \quad \tilde{\phi}^i \quad \tilde{M}_x{}^i \quad \tilde{V}_x{}^i \quad \tilde{S}_{x\theta}{}^i \quad \tilde{N}_x{}^i\right\}^T$ is the dimensionless state vector in the inner/outer shell. u, v, w and ϕ represent the axial displacement component, circumferential displacement component, radial displacement component and rotational angle, respectively. N_x, $S_{x\theta}$, V_x and M_x represent normal force, shear force, transverse force and moment, respectively. The overscored physical quantities represent the corresponding nondimensional state variables. $\boldsymbol{F}\left(\xi^i\right)$ and $\boldsymbol{p}\left(\xi^i\right)$ represent the external excitation and fluid load on the wet surface of the outer

shell, respectively. The nonzero element of the coefficient matrix $\mathbf{U}\left(\xi^i\right)$ is a function of ξ^i (Wang et al. 2016).

Both inner and outer shells are divided into *N* sections, in which the whole discrete points of the inner/outer shell along the axial direction can be written as $\xi_1^i \quad \xi_2^i \quad \xi_3^i \quad \cdots \quad \xi_N^i \quad \xi_{N+1}^i$ with step length $\Delta\xi^i$. Let $\boldsymbol{f}\left(\xi^i\right)$ satisfies $\boldsymbol{F}\left(\xi^i\right)-\boldsymbol{p}\left(\xi^i\right)$, the general solution of the first-order matrix differential equation can be written as follows

$$\boldsymbol{Z}\left(\xi_{j+1}^i\right)=\boldsymbol{T}_j^i\boldsymbol{Z}\left(\xi_j^i\right)+\boldsymbol{P}_j^i \quad , (1\leq j\leq N+1,\ i=1,2) \tag{2}$$

where $\boldsymbol{P}_j^i=\int_{\xi_j^i}^{\xi_{j+1}^i}e^{\int_{\tau^i}^{\xi_{j+1}^i}\boldsymbol{U}\left(\tau^i\right)d\tau}\boldsymbol{f}\left(\tau^i\right)d\tau$ is the Duhamel integral term of the external force vector of the inner/outer shell. $\boldsymbol{T}_j^i=\exp\left[\int_{\xi_j^i}^{\xi_{j+1}^i}\boldsymbol{U}\left(\tau^i\right)d\tau\right]\approx e^{\boldsymbol{U}^i\Delta\xi^i}$ are the field transfer matrices of j^{th} section of the inner/outer shell.

2.2 The annular plate

By considering the idea of simplifying the conical shell to be the annular plate, the field transfer matrix of a conical shell is borrowed to build the transfer relationship between both state vectors on the inner edge and outer edge of annular plate. When the cone apex angle α equals $\pi/2$, the transfer relationship between these two state vectors can be written as follows

$$\boldsymbol{Z}\left(\xi^2\right)=e^{\int_{\xi^1}^{\xi^2}\boldsymbol{U}_c d\tau}\boldsymbol{Z}\left(\xi^1\right) \tag{3}$$

where ξ^1, ξ^2 represent the dimensionless inside and outside radii of the conical shell. $\boldsymbol{U}_c$ is the coefficient matrix of the conical shell (Wang et al. 2016).

2.3 The stiffener

The state vector of the inner shell has a steep change at the position of the ring-stiffeners. The relationship between the state vector at the left section and the one at right section at a position ξ_k should satisfy

$$\boldsymbol{Z}\left(\xi_k^R\right)=\boldsymbol{T}r_k\boldsymbol{Z}\left(\xi_k^L\right) \tag{4}$$

where $\boldsymbol{Z}\left(\xi_k^L\right)$ and $\boldsymbol{Z}\left(\xi_k^R\right)$ are state vectors at the left section and the right section where the ring-stiffener is located

at, respectively. $\boldsymbol{Tr}_k$ is the point transfer matrix of order 8.

2.4 The dynamic load

The external excitation acting on the double-walled cylindrical shell can be simplified as distributed excitation f_i (i=1, 2…N). The i^{th} exciting load should be written as follows

$$f(x_i,\theta_i) = f_{0i}\delta(s_{0i})\delta(\theta_{0i})/R \tag{5}$$

where f_{0i} represents the amplitude of external excitation, s_{0i} represents the distributed range of external excitation along the meridian, θ_{0i} represents the distributed range of external excitation along the circumferential direction.

For a given wave number n, the external excitation can be written as follows

$$\boldsymbol{F} = RK^{-1}\begin{bmatrix}0 & 0 & 0 & 0 & 0 & f_n^r & f_n^c & f_n^a\end{bmatrix}^T \tag{6}$$

where f_n^r, f_n^c and f_n^a represent the radial, circumferential and axial excitations, respectively.

2.5 The vibro-acoustic responses

The sound pressure p^2 in external fluid satisfies the Sommerfeld boundary condition and the Helmholtz equation, which is different from sound pressure p^1 in the interlayer fluid. The sound pressure formula in both interlayer and external fluid field can be written as follows

$$p^1 = \sum_{n=0}^{\infty}\sum_{m=0}^{\infty}\left[a_{mn}F_n(k_r r) + b_{mn}G_n(k_r r)\right]\cos(k_m x)\cos(n\theta) \tag{7a}$$

$$p^2 = \sum_{n=0}^{\infty}\sum_{m=0}^{\infty}c_{mn}E_n(k_r r)\cos(k_m x)\cos(n\theta) \tag{7b}$$

where a_{mn}, b_{mn}, c_{mn} are the unsolved coefficients. k_m=$m\pi/L$ is the wavenumber in the meridian direction and $k_r = \sqrt{k_0^2 - k_m^2}$. k_0=ω/c_0 is the wavenumber of the fluid. c_0 is the sound speed in the fluid. ω is the angular frequency. When k_r is a real number, $E_n()$ is Hankel function of the second kind, $F_n()$ is a Bessel function, and $G_n()$ is a Neumann function. The Duhamel integral term $\boldsymbol{P}_j^{(1)}$ under generalized sound pressure loads $F_n(k_r r)\cos(k_m x)$ or

$G_n(k_r r)\cos(k_m x)$ can be obtained according to the solution procedure from literature (Wang et al. 2018).

The field transfer matrices $\boldsymbol{T}_j^{(i)}$ of the inner/outer shell are tackled by precise integration method (Zhong 2004). After assembling transfer relationships of both inner and outer shells, the general solution of the double-walled cylindrical shell can be written as follows

$$-\boldsymbol{T}_j\boldsymbol{Z}\left(\xi_j\right)+\boldsymbol{Z}\left(\xi_{j+1}\right)=\boldsymbol{P}_j \tag{8}$$

where $\boldsymbol{T}_j=\left\langle \boldsymbol{T}_j^{(1)} \quad \boldsymbol{T}_j^{(2)} \right\rangle$ is a 16×16 order field transfer matrix of the double-walled cylindrical shell. $\boldsymbol{Z}\left(\xi_j\right)$ represents the state vectors $\left\{\boldsymbol{Z}\left(\xi_j^{(1)}\right) \quad \boldsymbol{Z}\left(\xi_j^{(2)}\right)\right\}^T$ at $\xi=\xi_j$. Likewise, $\boldsymbol{Z}\left(\xi_{j+1}\right)$ equals $\left\{\boldsymbol{Z}\left(\xi_{j+1}^{(1)}\right) \quad \boldsymbol{Z}\left(\xi_{j+1}^{(2)}\right)\right\}^T$. $\boldsymbol{P}_j$ represents the force vectors $\left\{\boldsymbol{P}\left(\xi_j^{(1)}\right) \quad \boldsymbol{P}\left(\xi_j^{(2)}\right)\right\}^T$.

After assembling Eq. (4), Eq. (6), Eq. (7) and Eq. (8), the dynamic equations of the immersed ring-stiffened double-walled cylindrical shell can be expressed as follows

$$\begin{bmatrix} -\boldsymbol{T}_1 & \boldsymbol{I} & \boldsymbol{0} & \boldsymbol{0} & \boldsymbol{0} & \boldsymbol{0} \\ \boldsymbol{0} & -\boldsymbol{T}_2 & \boldsymbol{I} & \boldsymbol{0} & \boldsymbol{0} & \boldsymbol{0} \\ \boldsymbol{0} & \boldsymbol{0} & -\boldsymbol{T}_3 & \boldsymbol{I} & \boldsymbol{0} & \boldsymbol{0} \\ \boldsymbol{0} & \boldsymbol{0} & \boldsymbol{0} & \ldots & \boldsymbol{I} & \boldsymbol{0} \\ \boldsymbol{0} & \boldsymbol{0} & \boldsymbol{0} & \boldsymbol{0} & -\boldsymbol{T}_N & \boldsymbol{I} \end{bmatrix} \begin{Bmatrix} \boldsymbol{Z}\left(\xi_1\right) \\ \boldsymbol{Z}\left(\xi_2\right) \\ \boldsymbol{Z}\left(\xi_3\right) \\ \vdots \\ \boldsymbol{Z}\left(\xi_N\right) \end{Bmatrix} = \begin{Bmatrix} \boldsymbol{P}_1 \\ \boldsymbol{P}_2 \\ \vdots \\ \vdots \\ \boldsymbol{P}_N \end{Bmatrix} \tag{9}$$

After involving relevant given boundaries condition equations, the dispersion equation of the double-walled cylindrical shell is achieved from the determinant expansion of the coefficient matrix. Meanwhile, the state vectors $\boldsymbol{Z}(\xi)$ subjected to generalized sound pressure or the external load $\boldsymbol{F}(\xi)$ can be solved directly.

As to a given circumferential wavenumber *n*, the radial displacement of the shell satisfies the linear superposition principle

$$w^{(i)}(x)=w_f^{(i)}(x)+\sum_{m=1}^{\infty}\left(a_{mn}w_F^{(i)}(x)+b_{mn}w_G^{(i)}(x)+c_{mn}w_E^{(i)}(x)\right) \quad (i=1,2) \tag{10}$$

where $w_f^{(i)}(x)$, $w_E^{(i)}(x)$, $w_F^{(i)}(x)$ and $w_G^{(i)}(x)$ represent radial displacements subjected to external excitation $f(x_i, \theta_i)$, generalized sound pressure items $E_n(k_r r)\cos(k_m x)$, $F_n(k_r r)\cos(k_m x)$ and $G_n(k_r r)\cos(k_m x)$, respectively.

The radial displacement on the inner/outer shell surface and the sound pressure in fluid should satisfy the Neumann boundary condition, which can be written as follows

$$\frac{1}{i\omega\rho^{(1)}}\frac{\partial p^{(1)}}{\partial r}\Big|_{r=R_1}=\frac{\partial w^{(1)}}{\partial t}\Big|_{r=R_1} \tag{11a}$$

$$\frac{1}{i\omega\rho^{(1)}}\frac{\partial p^{(1)}}{\partial r}\Big|_{r=R_2}=\frac{\partial w^{(2)}}{\partial t}\Big|_{r=R_2} \tag{11b}$$

$$\frac{1}{i\omega\rho^{(2)}}\frac{\partial p^{(2)}}{\partial r}\Big|_{r=R_2}=\frac{\partial w^{(2)}}{\partial t}\Big|_{r=R_2} \tag{11c}$$

A total of M ($M>2\pi/\lambda$ & $M>m$) collocation points on the inner/outer shell are set up to get the displacement data. Eq. (7) and Eq. (10) are substituted into Eq. (11) to gain a set of linear algebraic equations, which is written as follows

$$\sum_{m=0}^{\infty} a_{mn}A_1+b_{mn}B_1+c_{mn}C_1=\rho^{(1)}\omega^2 w_f^{(1)}\left(x_m\right) \tag{12a}$$

$$\sum_{m=0}^{\infty} a_{mn}A_2+b_{mn}B_2+c_{mn}C_2=\rho^{(1)}\omega^2 w_f^{(2)}\left(x_m\right) \tag{12b}$$

$$\sum_{m=0}^{\infty} a_{mn}A_3+b_{mn}B_3+c_{mn}C_3=\rho^{(2)}\omega^2 w_f^{(2)}\left(x_m\right) \tag{12c}$$

The sound pressure in both outer fluid and interlayer fluid can be easily obtained by the Moore-Penrose pseudoinverse method to gain these unknown sound pressure coefficients a_{mn}, b_{mn} and c_{mn}.

2.6 Method verification

A steel high precision machining model is employed to validate the validity and reliability of the analytical model. The steel experiment model including shell parts and stiffeners parts has been manufactured by using the sophisticated NC milling machine to avoid the effect of welding. The machining cylindrical shell model is designed and made from Q235 steel, the material properties of which can be found in the literature (Wang et al. 2019). The function of the external hoisting model is achieved by welding the lifting lug at the end cover, as shown in Fig. 2(a). The boundary conditions of both ends of the cylindrical shell models are supposed to be clamped. Taking account of axisymmetric features, four measuring points are arranged on position 1(0.15, 30º, 0.35), position 2(0.15, 120º, 0.35), position 3(0.15, 0º, 0.448) and position 4(0.15, 0º, 0.546) to get the vibration acceleration data. Meanwhile, 2 Hydrophones are setup on hydrophone 1(1.0, -90º, 0.35) and hydrophone 2(1.2,

-114º, 0.35) to obtain the sound pressure data in an anechoic tank, as shown in Fig. 2(b).

The vibration acceleration level of the machining ring-stiffened cylindrical shell model in air is compared with that of the analytical model, as shown in Fig. 3(a), Fig. 3(b). The vibration acceleration level of the machining ring-stiffened cylindrical shell model in water is compared with that of the analytical model, as shown in Fig. 3(c), Fig. 3(d). Meanwhile, the sound pressure data in hydrophone 1 and hydrophone 2 are compared with the analytical results, as shown in Fig. 3(e), Fig. 3(f). It can be observed that in the measurement frequency band, the vibration response curves calculated by PTMM coincides very well with experimental curves, except some loss of resonance peaks in low frequency. This is due to the fact that the peak frequency is the natural frequencies of end caps of the test model. On the whole frequency range, the analytical results agree well with experimental results from frequency peaks to variation trend. In general, the sound pressure level of the test model is a little larger than the results from the analytical model. This is due to the local vibration of both thick end caps and seals flange, which contribute to the part of underwater acoustic radiation. The results from the analytical model are consistent with the test results, which proves that the present method is reliable to analyze the vibro-acoustic characteristics of the immersed cylindrical shell.

3 Experimental model

A ring-stiffened double-walled cylindrical shell is designed to complete a test model of steel structure, as shown in Fig. 4(a). This experimental model is scaled down based on actual submarines. Since there are many annular plates connecting the outer and inner shell of double-walled cylindrical shells, the three parts are welded together to manufacture the experimental model. The effect of welding is taken into consideration to compare with the relevant analytical model. Material properties and physical dimensions of the experimental model are provided in Table. 1. Both ends of the double-walled cylindrical shell are assembled by end covers and sealed with water sealant. The lifting lug is welded on the end cover to realize the purpose of suspending experimental model by the hoisting beam. Several test instruments including hammer, vibration exciter, primary sound source, station amplifier, forcing function generator, data acquisition unit, force transducer, acceleration sensors and hydrophones are employed to set up the vibration and acoustic measurement system. The underwater sound radiation is conducted in an anechoic tank, the size of which is 8 m×4 m×3 m(L×B×H). There are enough sound-absorption wedges placed on the walls and the cover of the anechoic tank, as shown in Fig. 4(b). The heavy load

is placed at the top cover of the experimental model to keep the hydrostatic balance.

The shaker (DH-40020) is screwed to an 8 mm square shim, which is welded on the internal surface of the inner shell of the experimental model. Also, the shaker is kept stationary by fixing on both end caps. A threaded rod between the patch and the shaker is involved to transfer the radial excitation. The section centre of the left end of the experimental model is defined as Cylindrical coordinates origin. The force excitation has been set with the amplitude 10N to obtain a higher signal to noise ratio (SNR). The cylindrical coordinates (x, θ, r) is employed to describe the experimental model, in which x represents the axial coordinate, θ represents the circumferential coordinate, and r represents the radial coordinate. The excitation point is located at the position (0.4m, 0.3m, 0). An impedance head (PCB-208C02) is placed on a threaded rod to gain the vibration acceleration data and output force data. The primary sound source (AH-AWA5510) is suspended in the middle of the experimental model by a flexible net. The experimental model hangs in air or water with a flexible rope, which relates to the shop crane. According to structure features, there are 10 sensors (PCB-352C03) placed to collect the vibration acceleration data as follows: sensor1 (0.4m, 0.3m, 0), sensor2 (0.48m, 0.3m, 0), sensor3 (0.56m, 0.3m, 0), sensor4 (0.4m, 0.3m, π/4), sensor5 (0.4m, 0.3m, π/2), sensor6 (0.4m, 0.3m, π), sensor7 (0.48m, 0.25m, 0), sensor8 (0.4m, 0.25m, π/4), sensor9 (0.4m, 0.25m, π/2) and sensor10 (0.4m, 0.25m, π).

4 Results and discussions

4.1 Free vibrations

The purpose in this section is to compare natural frequencies of the double-walled steel cylindrical shell from the experiment test with analytical values from PTMM. An impact hammer (PCB 086C03) is employed to tap on the experimental model, which is hoisted with a flexible rope. After stuck in the measurement points, the accelerometers (PCB 353B15) are employed to transfer the vibration acceleration data through the data acquisition system to the laptop. Both natural frequencies and structural modes are collected by the data analysis software in the test measurement system. In air case, the analytical model is assumed to be clamped and calculated to gain the natural frequencies. The experimental results are compared with corresponding natural frequencies of the analytical model with a high degree of accuracy, as shown in Table 2. The comparison shows that analytical results agree well with experimental results. The relative error is not more than 4%, which indicates PTMM is highly accurate and reliable. Besides the error in the manufacturing process, another main

reason of the error is that both ends of the experimental model are covered by the 15mm end caps, which is a little different with ideal clamped boundary conditions of the analytical model. Meanwhile, it also indicates that it is acceptable to ignore the influence of welding.

4.2 Forced vibration

Forced vibration tests subjected to the vibration exciter are performed in both air and water environment, as shown in Fig.5. In the test process, two frequency modes including a fixed frequency (10Hz-2500Hz) and a frequency sweep (100Hz, 125Hz, 160Hz, 200Hz, 250Hz, 315Hz, 400Hz, 500Hz, 630Hz, 800Hz, 1000Hz, 1250Hz, 1600Hz, 2000Hz, 2500Hz, 3150Hz, 4000Hz,) are generated from the signal generator as the input signal. The water density is 1000kg/m^3 and the sound velocity in water is 1500m/s. The vibration acceleration level L_a=20lg(a/a_0) is employed to evaluate the measured data of the acceleration sensors, where a is the vibration acceleration value and a_0 is the base acceleration value 1e-6 m/s^{-2}.

In air case, the vibration acceleration level at measurement points is gained by processing acceleration data in the whole frequency range. The boundary condition at both ends of the analytical model is still assumed to be clamped to approximately simulate the real situation. The forced vibration response of the analytical model under a frequency sweep excitation is compared with experimental results, as shown in Fig.6. Within the 100 Hz to 500 Hz range, these two response curves are obviously different at the resonance peak value, especially those at some measuring points of the outer shell. The welding quality of the junction of the experimental model affects the transmission of vibration energy from the inner shell to the outer shell, which results in the difference of the resonance peak value. The response curves of the analytical model are smoother than the test curves. The local vibration modes of end caps of the experimental model do not exist in the analytical model. The considerable difference in sensor3 is mainly because of the boundary condition. The position of measuring point sensor3 is too close to the end of the outer shell, which is fixed by the bolts. Within the 1000 Hz to 2500 Hz range, there is a loss of some resonance peaks and a slight difference in frequency peak values. It is mainly due to the local vibration of end covers and seals flanges, which are not taken into consideration in the analytical model. In addition, Fig.7 presents the comparison of the forced vibration acceleration value between experimental results and PTMM results under fixed frequencies excitation. Within the 100 Hz to 1000 Hz range, the vibration acceleration level at measurement points on the outer shell are close to those of measurement points on the inner shell. This is because the vibration wavelength at low frequency is much longer than the principal dimensions of the structure, which results in the whole vibration of the double-walled cylindrical shell. However, the vibration acceleration level of measurement points on the outer shell is larger than those of measurement points on the inner shell in the 1kHz to 4kHz band. In general, the vibration acceleration results of the analytical model from PTMM agree well with the trend of the test curves in the 100~2500Hz band, which proves that the PTMM is reliable and

credible.

In water case, Fig.8 presents the forced vibration response of immersed experimental model under a frequency sweep excitation. Fig.9 presents the comparison of the vibration acceleration value between experimental results and PTMM results under fixed frequencies excitation. The comparative analysis shows that the vibration response curve from PTMM coincides with the vibration curve of the experimental results. Within the 100 Hz to 800 Hz range, there is little difference in vibration levels at different locations. The vibration responses of the whole sensors on the inner shell are always larger than those of sensors on the outer shell. At some fixed frequencies, the difference between experimental results and analytical results at some positions is obvious. One of the important reasons is that the simulation of acoustic-structure coupling. Compared with the test model completely immersed in water, the analytical model employed sound pressure formulas to simulate the fluid load with the hypothesis that the sound pressure gradients at both ends are zero. Another reason is the contribution of the local vibration energy of seal flanges and end covers on the sound radiation, which is not taken into consideration in the analytical model. Also, the vibration difference of the outer shell between the analytical model and experimental model certainly results in the difference of the acoustic responses of both models.

4.3 Acoustic radiation

The forcing function generator generates a sinusoidal input signal as a frequency sweep excitation to drive the vibration exciter and the dodecahedron sound source to excite the immersed experimental model, as shown in Fig.10. Then the radiated noise resulted from the vibration energy of the wet surface of the outer shell of the experimental model. There are 3 hydrophones (BK-8104) placed in the underwater anechoic tank to collect the radiated noise data, which are placed 1.0 meter away from the wet surface of the outer shell, as shown in Fig.1c). Under different excitations with the linear sweep frequency (100Hz-2500Hz), the sound pressure value is converted into the sound pressure level by $L_p=20\lg(p/p_0)$, where p is the experimental value and p_0 is the base acceleration value 1 μp_a.

In the force excitation case, the comparison of the radiated noise L_p between PTMM results and the experimental results is shown in Fig.11. In the acoustic excitation case, the comparison of the radiated noise L_p between PTMM results and the experimental results is shown in Fig.12. In the acoustic and force excitation case, the exciter and sound source operate under the same input voltage. The comparison of the radiated noise L_p between PTMM results and the experimental results is shown in Fig.13. Although the sound pressure level L_p is obviously different at the resonance peak values of response curves in 100 Hz ~800Hz range, the radiated noise value of analytical model coincides basically with the test results. The fluctuation of the sound pressure level is mainly due to the local vibration of both end caps in the low-frequency band. The PTMM result loss some resonance peaks compared with the test curve at 1500-2500Hz frequency range. In sound source excitation case,

the coupling between acoustic cavity mode and structural mode affects the sound radiation of the double-walled cylindrical shell if the interior of the experimental model is air. However, only the structural vibration mode is involved in the sound radiation of the analytical model. The cut-off frequency of the anechoic tank is 4kHz, which means that the sound reflection of an anechoic tank cannot be neglected in the measurement frequency range. Another interference factor is the sound transmission of airborne sound from the sound source.

Comparison of sound pressure level under fixed frequencies excitation is shown in Fig.14. After a comprehensive analysis, there is still a significant difference in peak frequencies and peak numbers under different excitations. In low-frequency range 100Hz to 400Hz, some frequency peaks only exist in the force excitation case. Under the sound source excitation, the sound pressure level L_p is much larger than those under the force excitation. Under the combined excitation, the sound pressure level L_p tends to coincide with those under the acoustic excitation, which indicates that the acoustic excitation plays a leading role in the low-frequency band. However, some frequency peaks only exist in sound source excitation case in 400Hz to 2500Hz frequency range. Under the acoustic excitation, the sound pressure level L_p is lower than those under the force excitation. The sound pressure level L_p under the combined excitation tends to coincide with those under the force excitation, which indicates that the force excitation is a major contributor in the middle-high frequency band. This also indicates that the frequency peaks are only relevant to structural modes in the force excitation case. The frequency peaks are relevant to structural modes and internal cavity modes under the acoustic excitation.

4.4 Effects of restraints stiffnesses

The effect of boundary restraints stiffnesses of the double-walled cylindrical shell on the underwater sound radiation is analyzed. The effect of axial restraints stiffness k_u, tangential restraints stiffness k_v and radial restraints stiffnesses k_w on the sound pressure level are discussed and shown in Fig. 15, Fig. 16 and Fig. 17, respectively. These curves of various axial restraints stiffnesses are almost overlapped in 10Hz-450 Hz, whether the inner shell or outer shell with the elastic boundary. When the inner shell is setup with the elastic boundary, the peak frequencies are quite different in 450Hz-1200Hz. However, there is a slight difference only existed in peak values. The response curves are slightly separated but the trend is consistent in 1200Hz-2kHz. Whether the inner shell or the outer shell elastic boundary, the sound pressure level curves under different tangential restraints stiffnesses have a significant difference in 10Hz-1200Hz. Similarly, the radial restraint stiffness has an effective effect on the peak values in 10Hz-1200 Hz. Nevertheless, the restraint stiffness has relatively few effects on the sound pressure curves in 1200Hz-2kHz, the trend of which is basically the same. In general, the effect of restraint stiffness is a bigger impact on the sound pressure level while the inner shell is setup with the elastic boundary in 1200Hz-2kHz.

Conclusions

In this paper, the experimental model of a ring-stiffened double-walled cylindrical shell under different excitations is designed to perform vibration and acoustic test under the linear sweep frequency excitation and the fixed frequency excitation. The purpose of the experimental test is to gain the natural frequencies, forced vibration responses in air and water, radiated noise in water. Based on PTMM, the analytical model for vibration and sound radiation of double-walled cylindrical shells is also established to gain natural frequencies, vibration acceleration level L_a in vacuo and water, sound pressure level L_p in water. Then the comparison of vibro-acoustic responses between experimental results and PTMM results are discussed. The main conclusions can be summarized as follows:

(1) Compared the natural frequencies and vibration acceleration shows that PTMM is effective and reliable to predict the vibration responses of the stiffened double-walled cylindrical shell.

(2) The acoustic responses of the double-walled cylindrical shell from PTMM is basically consistent with experimental results. It proves that the analytical model is credible to assess the acoustic radiation level of the stiffened double-walled cylindrical shell. Approximation error of sound pressure formulas, assumed boundary conditions and the neglect of acoustic cavity modes are the main reason for the difference.

(3) In the force excitation case, the peak value of radiated noise is relevant to structural modes. Whereas it is relevant to structural modes and cavity modes in the acoustic excitation case. The acoustic excitation plays a leading role in the low-frequency range. However, the force excitation is a major contributor to the middle-high frequency band.

(4) The effect of boundary restraints stiffnesses on the sound pressure level was concentrated in 10Hz-1200 Hz. When the inner shell is setup with the elastic boundary, the effect of restraint stiffness is a bigger impact on the sound pressure level in 1200Hz-2kHz.

Acknowledgements

The authors would like to thank the anonymous reviewers for their very valuable comments. This paper was financially supported by the National Natural Science Foundation of China (No. 51779201), China Scholarship Council (201806955052) and Nature Science Foundation of Hubei Province (2018CFB607).

References

Bai, Z., (2012). Analysis on transmission of sound and vibration of underwater double cylindrical shells connected with noncontinuous slab ribs. *The Journal of the Acoustical Society of America*, *131*(4), 3528-3528.

Caresta, M., Kessissoglou, N.J., (2009). Structural and acoustic responses of a fluid-loaded cylindrical hull with structural discontinuities. *Applied Acoustics*, *70*(7), 954-963.

Caresta, M., Kessissoglou, N.J., (2009). Purely axial vibration of thin cylindrical shells with shear-diaphragm boundary conditions. *Applied Acoustics*, *70*(8), 1081-1086.

Chen, M., Xie, K., Jia, W., Xu, K., (2015). Free and forced vibration of ring-stiffened conical–cylindrical shells with arbitrary boundary conditions. *Ocean Engineering*, *108*(1), 241-256.

Chen, M., Zhang, L., Xie, K., (2018). Vibration analysis of a cylindrical shell coupled with interior structures using a hybrid analytical-numerical approach. *Ocean Engineering*, *154*81-93.

Chen, Y., Jin, G., Liu, Z., (2013). Free vibration analysis of circular cylindrical shell with non-uniform elastic boundary constraints. *International Journal of Mechanical Sciences*, *74*120-132.

De Faria, A., (2004). Finite element analysis of the dynamic response of cylindrical panels under traversing loads. *European Journal of Mechanics-A/Solids*, *23*(4), 677-687.

Ettouney, M.M., Daddazio, R.P., Abboud, N.N., (1994). The interaction of a submerged axisymmetric shell and three-dimensional internal systems. *International journal for numerical methods in engineering*, *37*(17), 2951-2970.

Everstine, G., (1997). Finite element formulatons of structural acoustics problems. *Computers & Structures*, *65*(3), 307-321.

Everstine, G.C., Henderson, F.M., (1990). Coupled finite element/boundary element approach for fluid–structure interaction. *The Journal of the Acoustical Society of America*, *87*(5), 1938-1947.

Gan, L., Li, X., Zhang, Z., (2009). Free vibration analysis of ring-stiffened cylindrical shells using wave propagation approach. *Journal of Sound and Vibration*, *326*(3-5), 633-646.

Irie, T., Yamada, G., Muramoto, Y., (1984). Free vibration of joined conical-cylindrical shells. *Journal of Sound and Vibration*, *95*(1), 31-39.

Jafari, A., Bagheri, M., (2006). Free vibration of non-uniformly ring stiffened cylindrical shells using analytical, experimental and numerical methods. *Thin-Walled Structures*, *44*(1), 82-90.

Jin, G., Ma, X., Liu, Z., Xuan, L., (2017). Dynamic Analysis of General Rotationally Symmetric Built-Up Structures Using a Modified Fourier Spectral Element Approach. *Journal of Vibration and Acoustics*, *139*(2), 021012.

Liang, X., Zha, X., Jiang, X., Cao, Z., Wang, Y., Leng, J., (2019). A semi-analytical method for the dynamic analysis of cylindrical shells with arbitrary boundaries. *Ocean Engineering*, *178*, 145-155.

Liu, C.-H., Chen, P.-T., (2009). Numerical analysis of immersed finite cylindrical shells using a coupled BEM/FEM and spatial spectrum approach. *Applied Acoustics*, *70*(2), 256-266.

Ma, X., Jin, G., Shi, S., Ye, T., Liu, Z., (2017). An analytical method for vibration analysis of cylindrical shells coupled with annular plate under general elastic boundary and coupling conditions. *Journal of Vibration and Control*, *23*(2), 305-328.

Meyer, V., Maxit, L., Guyader, J.-L., Leissing, T., (2016). Prediction of the vibroacoustic behavior of a submerged shell with non-axisymmetric internal substructures by a condensed transfer function method. *Journal of Sound and Vibration*, *360*, 260-276.

Mukhopadhyay, M., Sinha, G., (1992). A review of dynamic behavior of stiffened shells. *The Shock and vibration digest*, *24*(8), 3-13.

Park, J. H., Bae, D., Oh, C. K., (2016). Experimental study on the dynamic behavior of a cylindrical liquid storage tank subjected to seismic excitation. *International Journal of Steel Structures*, *16*(3), 935-945.

Qu, Y., Chen, Y., Long, X., Hua, H., Meng, G., (2013). A modified variational approach for vibration analysis of ring-stiffened conical–cylindrical shell combinations. *European Journal of Mechanics-A/Solids*, *37*, 200-215.

Rawat, A., Matsagar, V.A., Nagpal, A.K., (2019) Free Vibration Analysis of Thin Circular Cylindrical Shell with Closure Using

Finite Element Method. *International Journal of Steel Structures*, 5, 1-19.

Ruotolo, R., (2001). A comparison of some thin shell theories used for the dynamic analysis of stiffened cylinders. *Journal of Sound and Vibration*, *243*(5), 847-860.

Su, Z., Jin, G., (2016). Vibration analysis of coupled conical-cylindrical-spherical shells using a Fourier spectral element method. *The Journal of the Acoustical Society of America*, *140*(5), 3925-3940.

Temami, O., Ayoub, A., Hamadi D., (2019) Effect of Boundary Conditions on the Behavior of Stiffened and Un-Stiffened Cylindrical Shells. *International Journal of Steel Structures*, *19*(3), 867-878.

Tso, Y., Hansen, C., (1995). Wave propagation through cylinder/plate junctions. *Journal of Sound and Vibration*, *186*(3), 447-461.

Ventsel, E., Naumenko, V., Strelnikova, E., Yeseleva, E., (2010). Free vibrations of shells of revolution filled with a fluid. *Engineering analysis with boundary elements*, *34*(10), 856-862.

Wang, X., Chen, D., Xiong, Y., Jiang, Q., Zuo, Y., (2018). Experiment and modeling of vibro-acoustic response of a stiffened submerged cylindrical shell with force and acoustic excitation. *Results in Physics*, *11*, 315-324.

Wang, X., Guo, W., (2016). Dynamic modeling and vibration characteristics analysis of submerged stiffened combined shells. *Ocean Engineering*, *127*, 226-235.

Wang, X., Wu, W., Yao, X., (2015). Structural and acoustic response of a finite stiffened conical shell. *Acta Mechanica Solida Sinica*, *28*(2), 200-209.

Wang, X.Z., Jiang, C.B., Xu, R.Y., (2016). Structural and acoustic response of a finite stiffened submarine hull. *China Ocean Engineering*, *30*(6), 898-915.

Wang, X.Z., Chen, D., Xiong, Y.P., Wu, W.G., (2019) Simulation and investigations on the vibro-acoustic behavior of cylindrical shells in ice-covered water. *Results in Physics*, 15, 1-11.

Xie, K., Chen, M., (2018). Wave based method for vibration analysis of double-walled cylindrical shells. *Applied Acoustics*, *139*, 293-306.

Xuebin, L., (2008). Study on free vibration analysis of circular cylindrical shells using wave propagation. *Journal of Sound and Vibration*, *311*(3-5), 667-682.

Yamada, G., Irie, T., Tamiya, T., (1986). Free vibration of a circular cylindrical double-shell system closed by end plates. *Journal of Sound and vibration*, *108*(2), 297-304.

Zhang, C., Shang, D.J., Li, Q., (2013). Prediction for Sound Radiated Power from Submerged Double Cylindrical Shells Based on Measuring Vibration of Inner Shell. *Advanced Materials Research*, *779*, 602-606.

Zhang, G., Li, T., Zhu, X., Yang, J., Miao, Y., (2017). Free and forced vibration characteristics of submerged finite elliptic cylindrical shell. *Ocean Engineering*, *129*, 92-106.

Zhang, Q., Mao, Y., Qi, D., (2017). Effect of perforation on the sound transmission through a double-walled cylindrical shell. *Journal of Sound and Vibration*, *410*, 344-363.

Zhong, W.X., (2004). On precise integration method. *Journal of Computational and Applied Mathematics*, *163*(1), 59-78.

Table Captions

Table. 1 Physical dimension and material properties of the experimental model

Geometrical and Physical parameters		Value
The radius	Inner shell R_1	0.25m
	Outer shell R_2	0.3m
The thickness	Inner shell h_1	4 mm
	Outer shell h_2	4 mm
Length L		0.8m
the height of the annular plate h_a		50mm
the thickness of the annular plate t_a		4mm
The annular plate spacing Δl		0.16m
Ring rib $h_r \times t_r$		40mm × 4mm
The stiffeners spacing Δl		0.16m
Density (kg/m^3)		7850kg/m^3
Elastic modulus (Pa)		203GPa
Poisson's ratio		0.3
Damping		0.01

Table. 2 Comparison of natural frequencies of the double-walled cylindrical shell (unit：Hz)

Mode (m, n)	(1,2)	(1,3)	(2,3)	(2,2)	(3,3)	(1,4)	(2,4)	(3,4)	(4,4)	(1,5)
Experimental Results	599.1	826.6	1242.7	1299.5	1362.2	1464.5	1472.8	1605.7	1622.1	1731.7
PTMM Results	599.4	831.8	1290.2	1297.7	1397.7	1429.8	1432.2	1662.2	1693.1	1750.9
Error (%)	0.1	0.6	3.7	0.1	2.5	2.4	2.8	3.4	4.2	1.1

Figure Captions

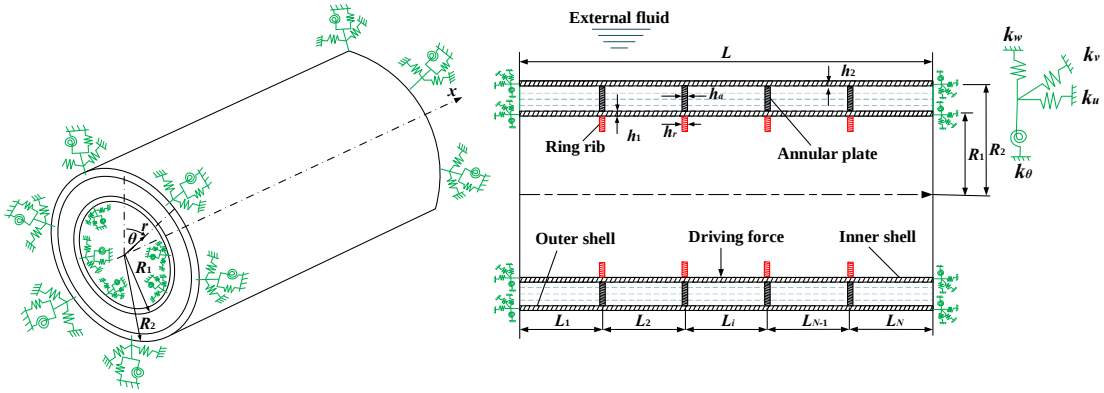

Fig.1 Schematic diagram of the immersed stiffened double-walled cylindrical shell

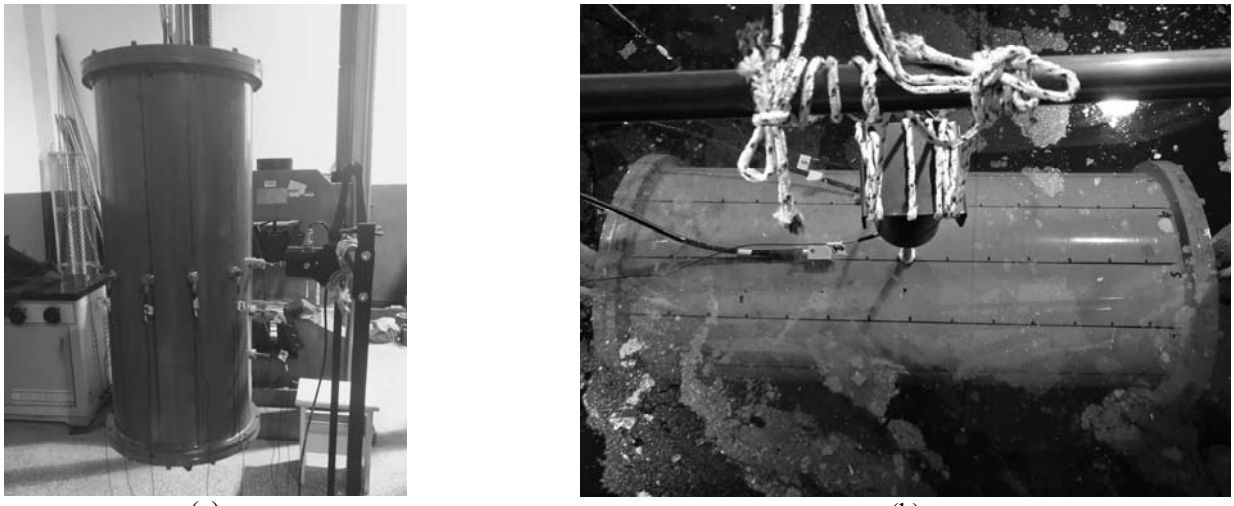

(a) (b)

Fig.2 Experiment test of the verification model: (a) vibration test in air, (b) vibro-acoustic test in water

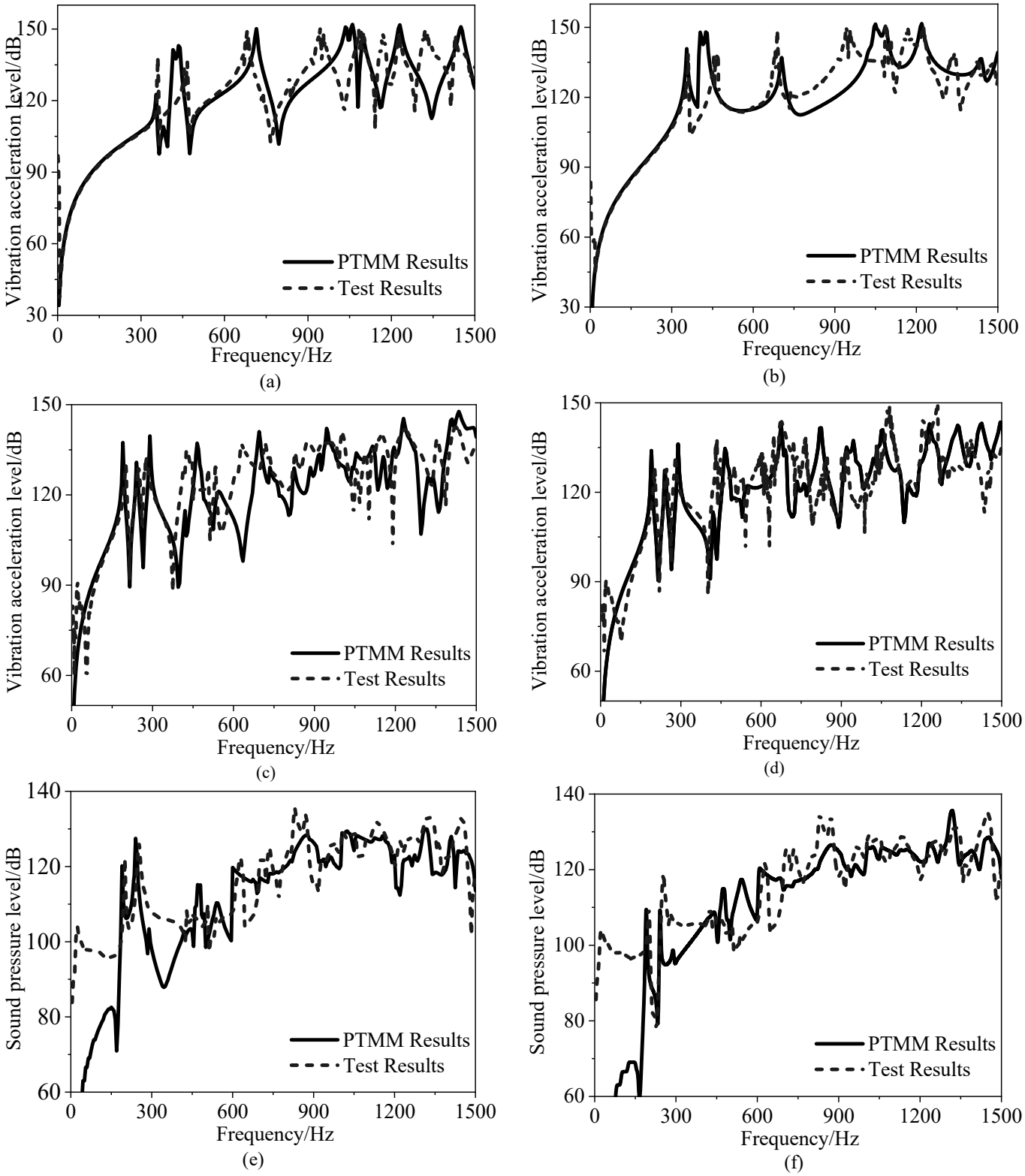

Fig.3 Comparison curves of experimental results and numerical results: (a) position 1, (b) position 2, (c) position 3, (d) position 4, (e) hydrophone 1, (f) hydrophone 2

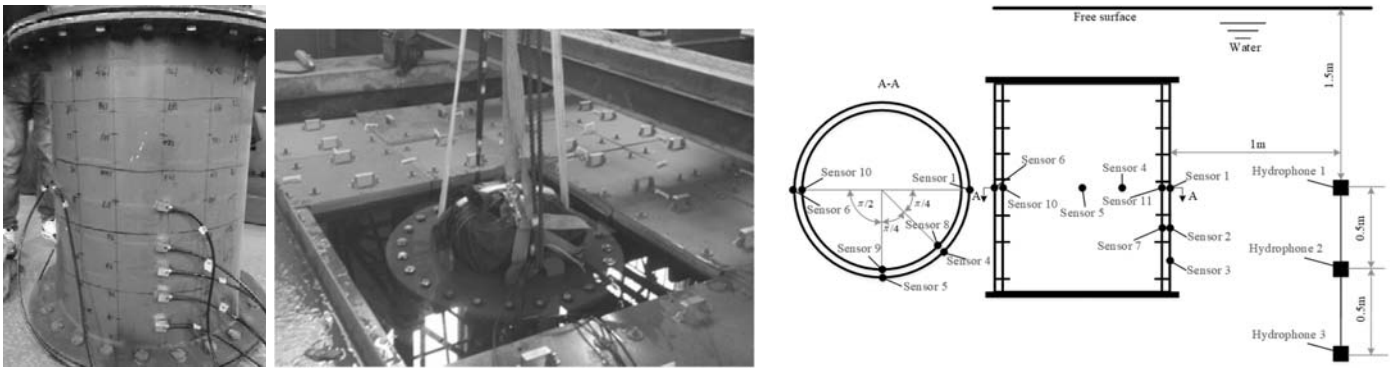

(a) (b) (c)

Fig.4. Pictures of the double-walled steel cylindrical shell: (a) hanged on a rope, (b) immersed in anechoic tank, (c) the layout of measuring points

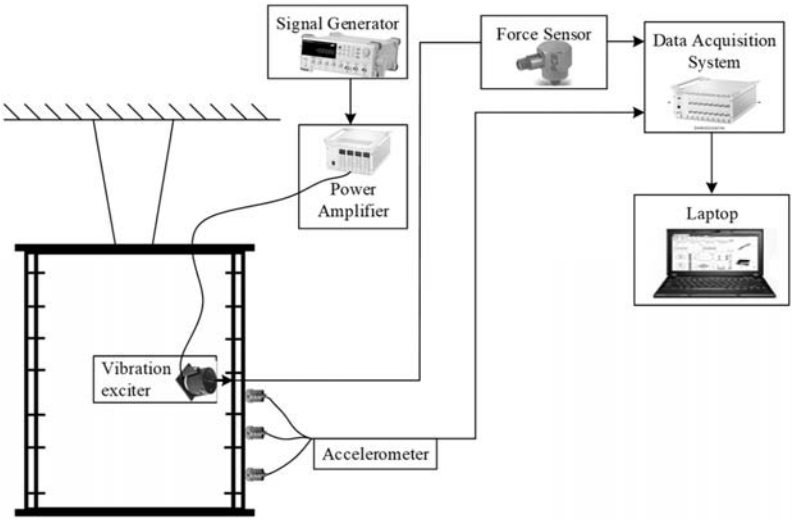

Fig.5 Forced vibration test system of the experimental model in air case

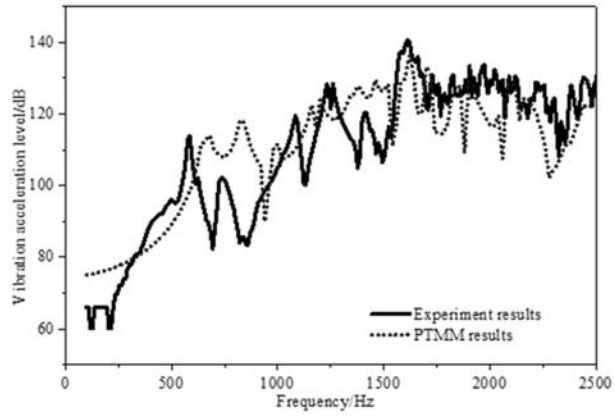
Vibration acceleration level/dB
Frequency/Hz
Experiment results
PTMM results

(a)

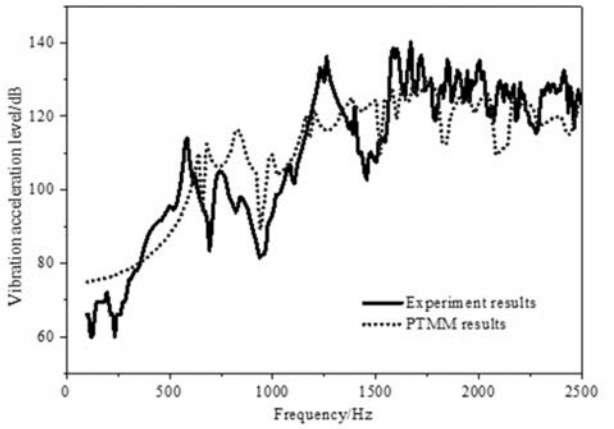
Vibration acceleration level/dB
Frequency/Hz
Experiment results
PTMM results

(b)

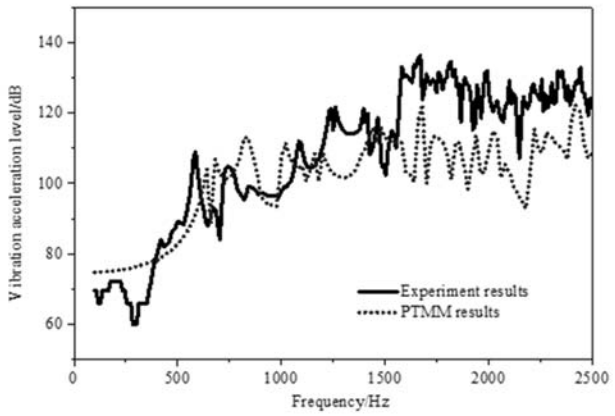
Vibration acceleration level/dB
Frequency/Hz
Experiment results
PTMM results

(c)

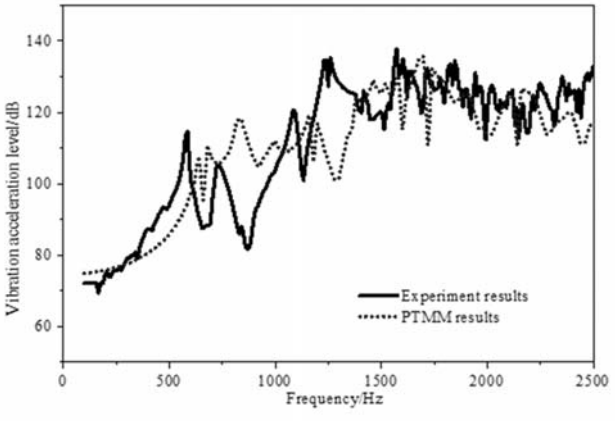
Vibration acceleration level/dB
Frequency/Hz
Experiment results
PTMM results

(d)

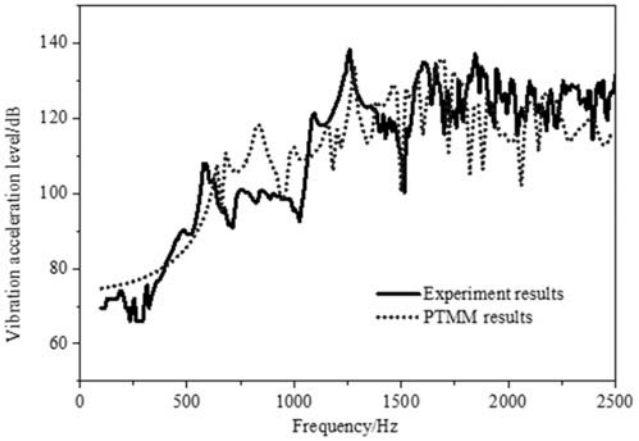
Vibration acceleration level/dB
Frequency/Hz
Experiment results
PTMM results

(e)

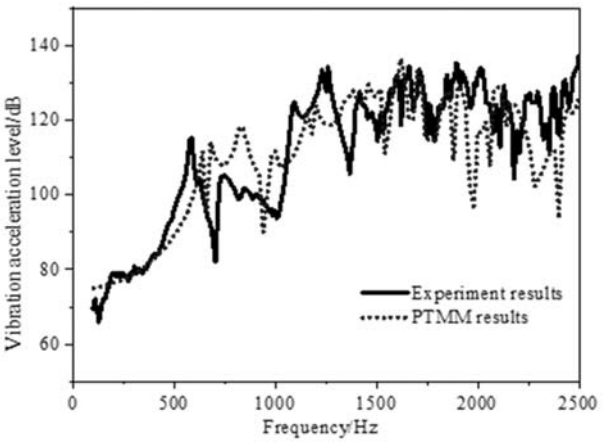
Vibration acceleration level/dB
Frequency/Hz
Experiment results
PTMM results

(f)

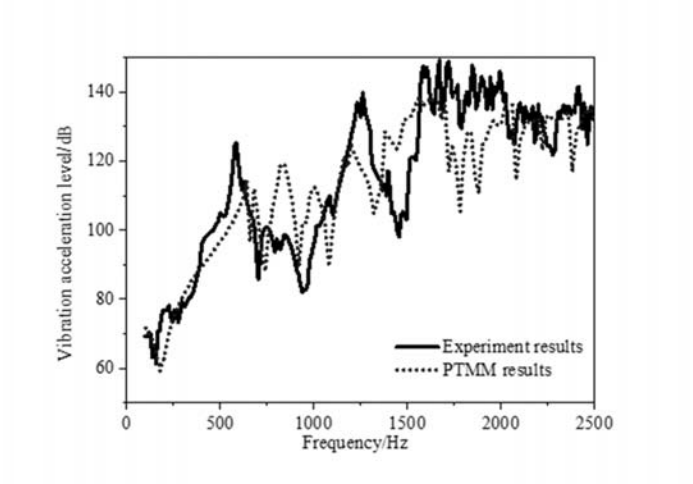

(g)

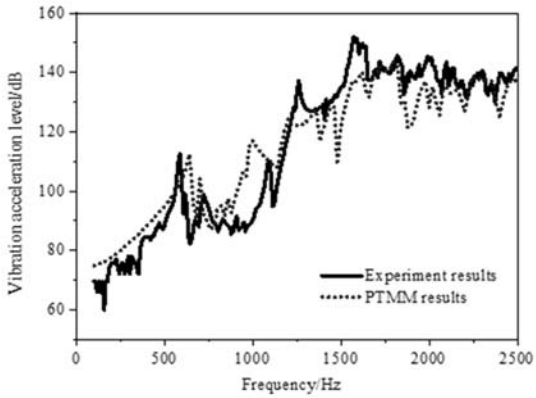

(h)

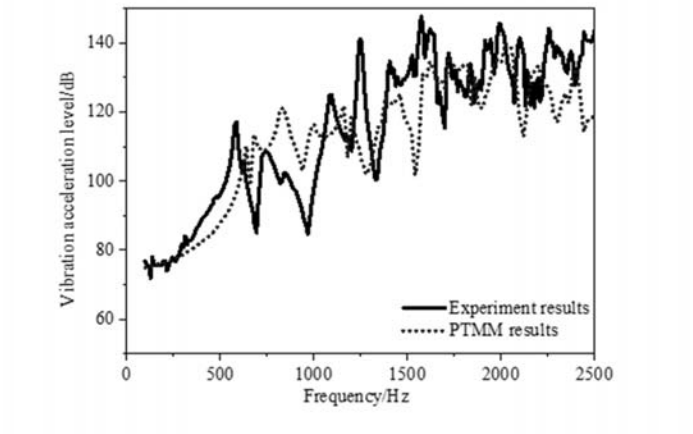

(i)

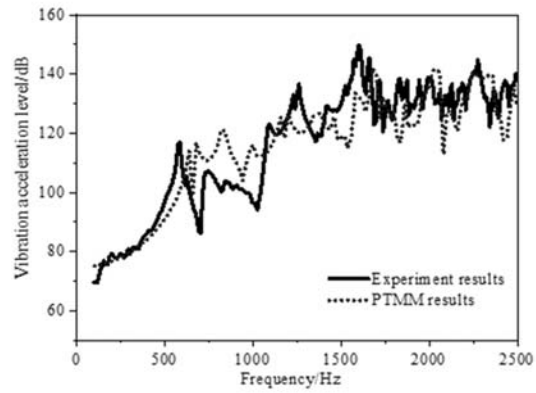

(j)

Fig.6 Forced vibration responses in air: (a) Sensor1, (b) Sensor2, (c) Sensor3, (d) Sensor4, (e) Sensor5, (f) Sensor6, (g) Sensor7, (h) Sensor8, (i) Sensor9, (j) Sensor10

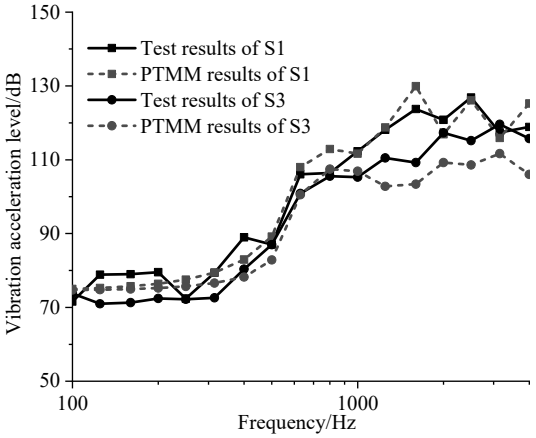

(a)

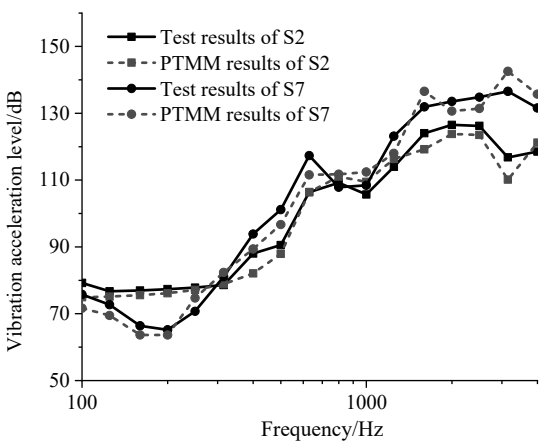

(b)

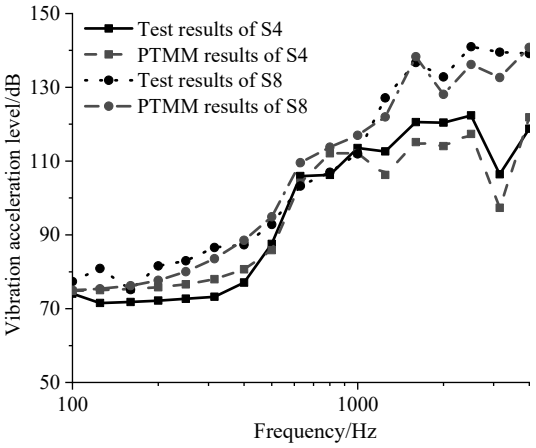

(c)

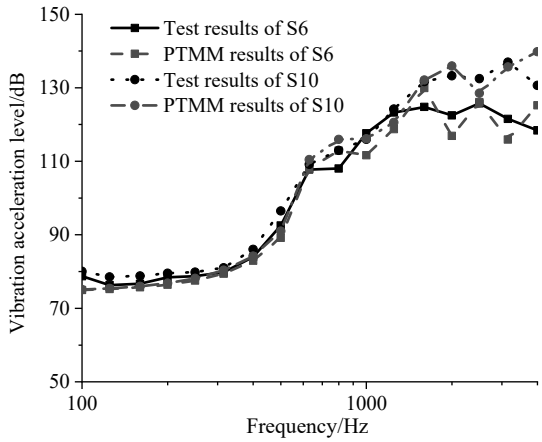

(d)

Fig.7 Vibration results with fixed frequency in air: (a) Sensor1 and Sensor3, (b) Sensor2 and Sensor7, (c) Sensor4 and Sensor8, (d) Sensor6 and Sensor10

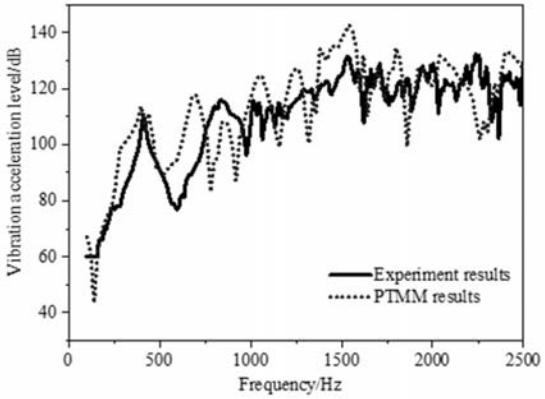
Vibration acceleration level/dB
Frequency/Hz
Experiment results
PTMM results

(a)

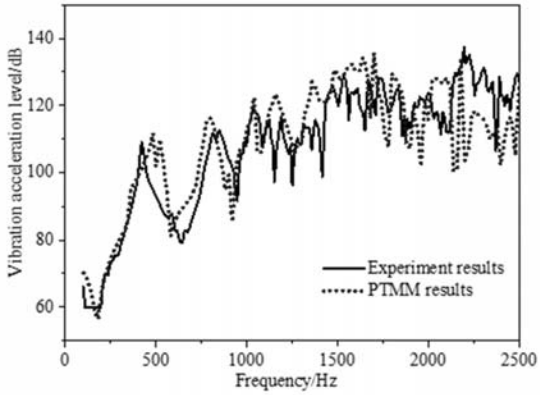
Vibration acceleration level/dB
Frequency/Hz
Experiment results
PTMM results

(b)

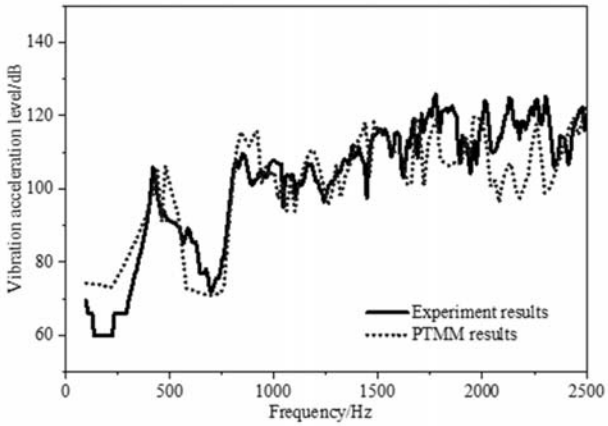
Vibration acceleration level/dB
Frequency/Hz
Experiment results
PTMM results

(c)

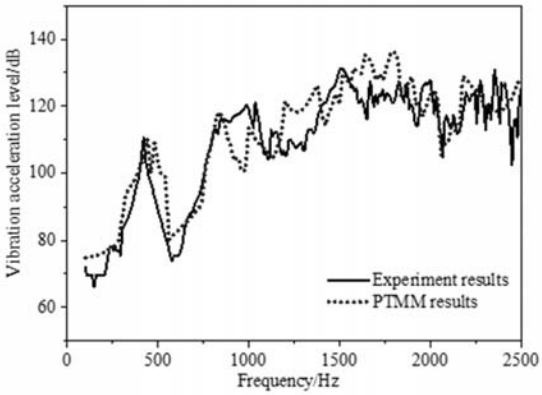
Vibration acceleration level/dB
Frequency/Hz
Experiment results
PTMM results

(d)

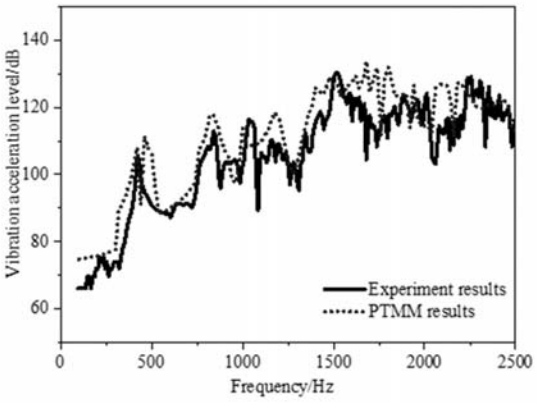
Vibration acceleration level/dB
Frequency/Hz
Experiment results
PTMM results

(e)

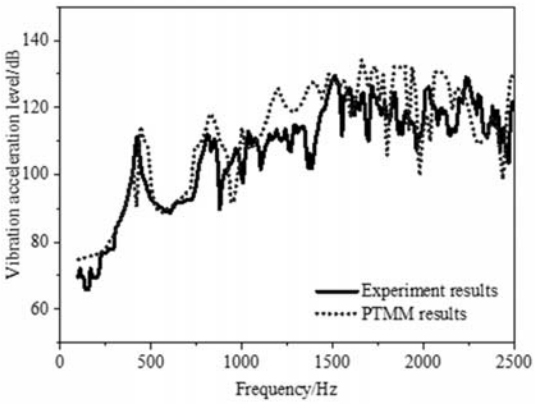
Vibration acceleration level/dB
Frequency/Hz
Experiment results
PTMM results

(f)

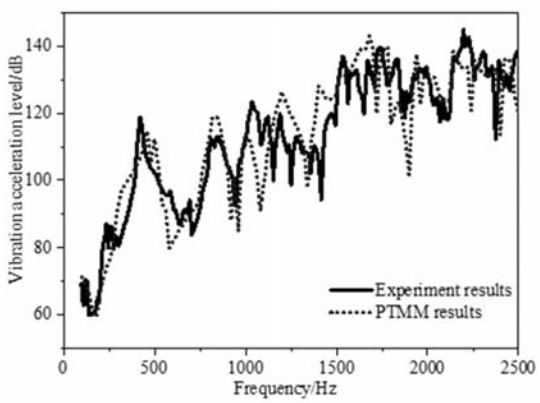

(g)

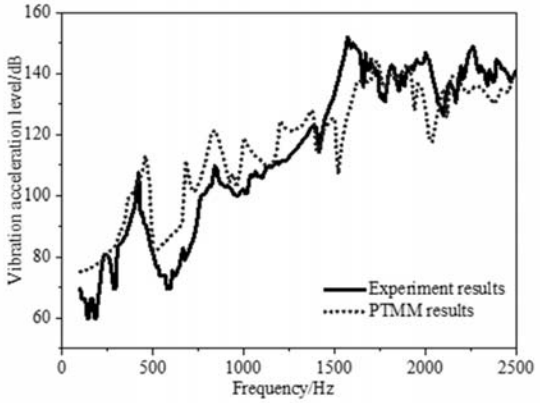

(h)

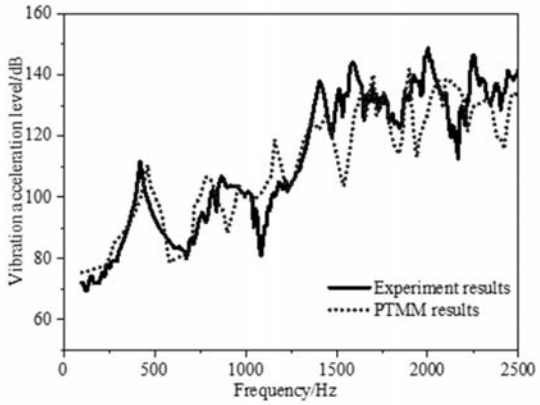

(i)

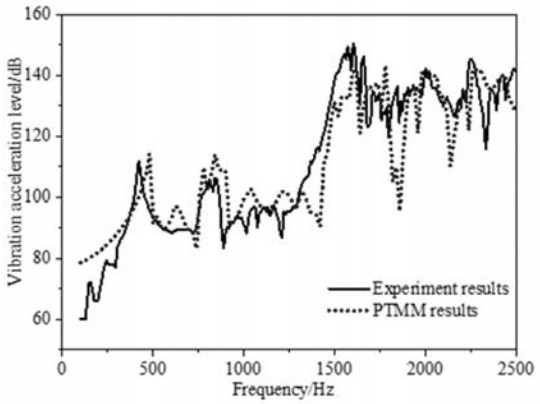

(j)

Fig.8 Forced vibration responses in water: (a) Sensor1, (b) Sensor2, (c) Sensor3, (d) Sensor4, (e) Sensor5, (f) Sensor6, (g) Sensor7, (h) Sensor8, (i) Sensor9, (j) Sensor10

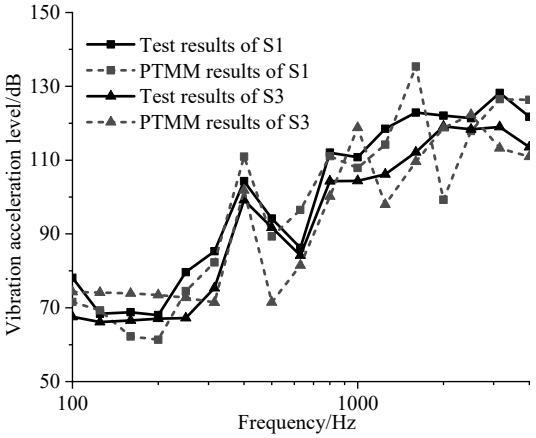

(a)

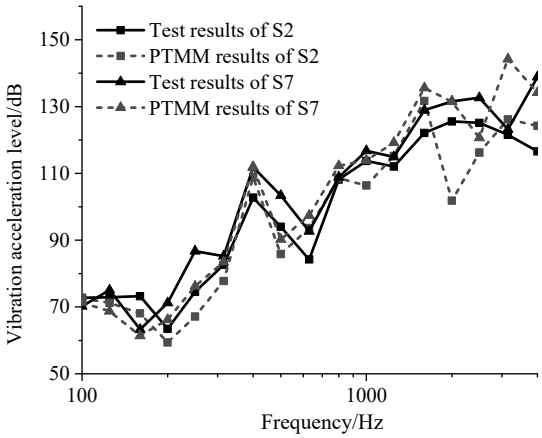

(b)

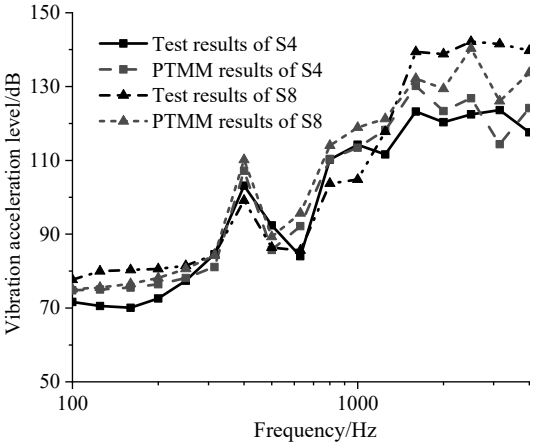

(c)

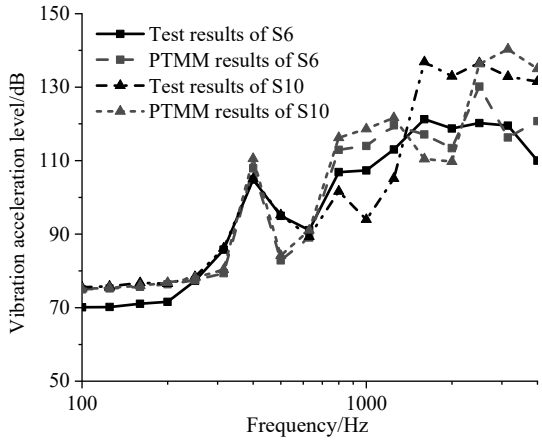

(d)

Fig.9 Vibration results with fixed frequency in water: (a) Sensor1 and Sensor3, (b) Sensor2 and Sensor7, (c) Sensor4 and Sensor8, (d) Sensor6 and Sensor10

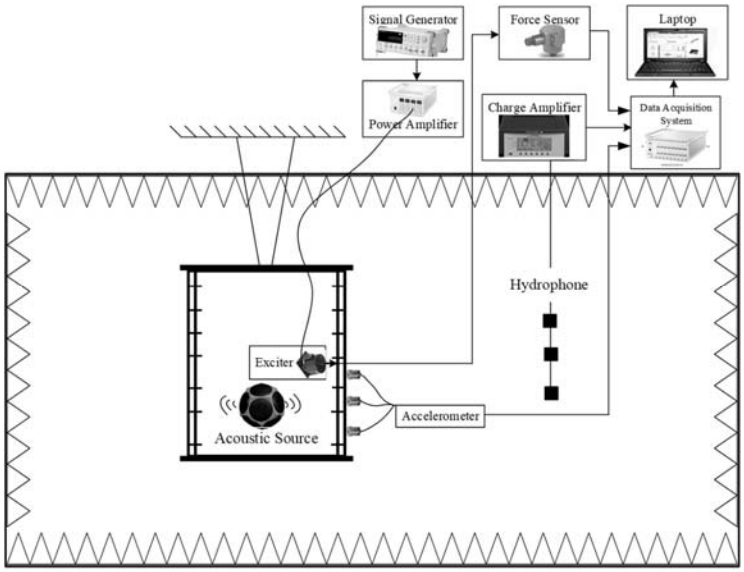

Fig.10 Sound pressure test system of the experimental model in an anechoic tank

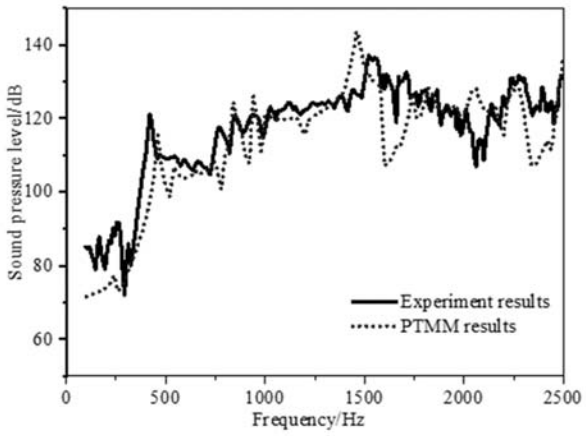

(a)

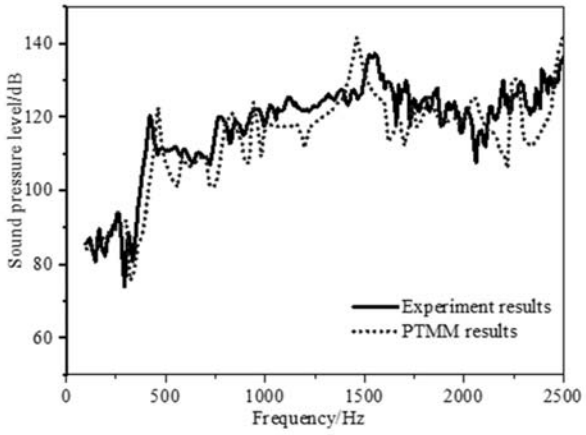

(b)

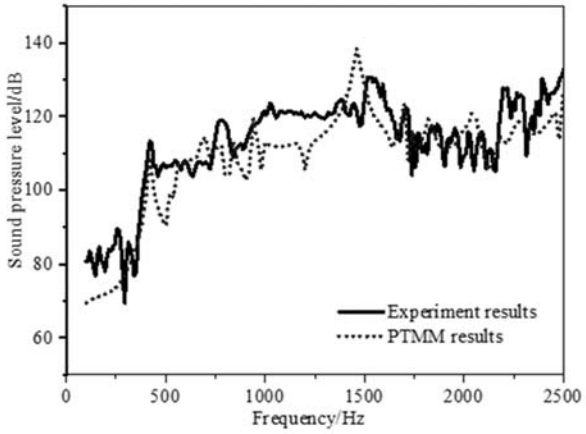

(c)

Fig.11 The underwater sound pressure in force excitation case: (a) hydrophone 1, (b) hydrophone 2, (c) hydrophone 3

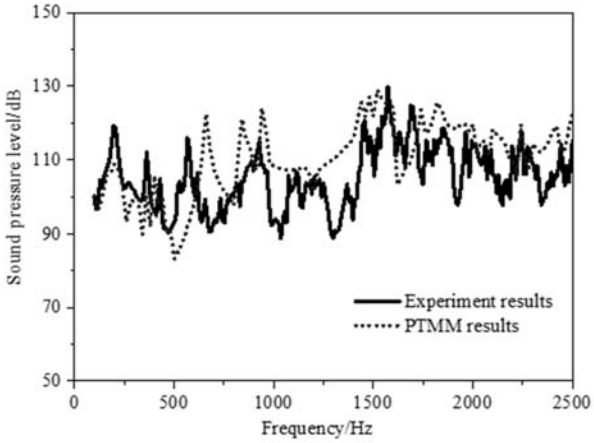

(a)

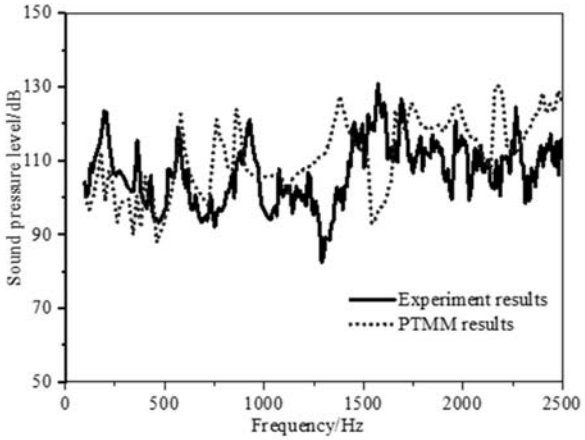

(b)

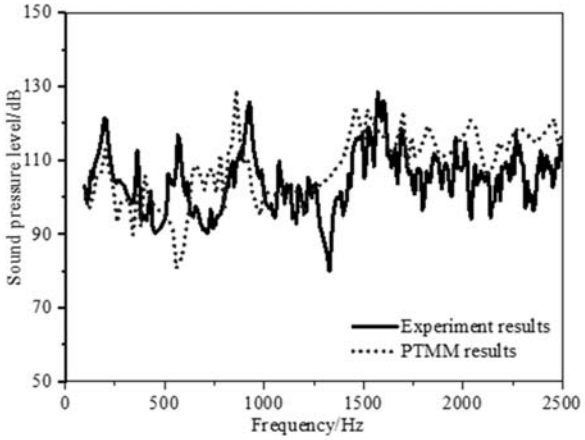

(c)

Fig.12 The underwater sound pressure in acoustic excitation case: (a) hydrophone 1, (b) hydrophone 2, (c) hydrophone 3

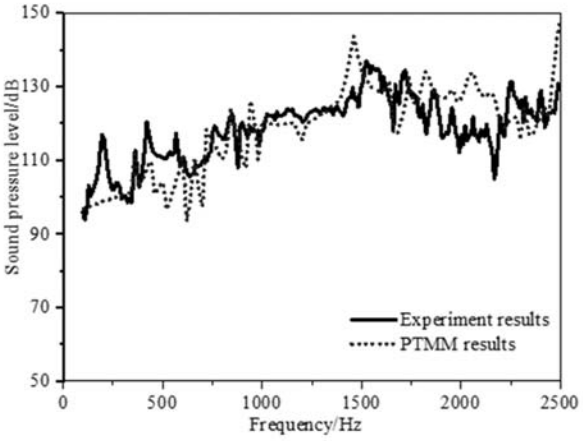

(a)

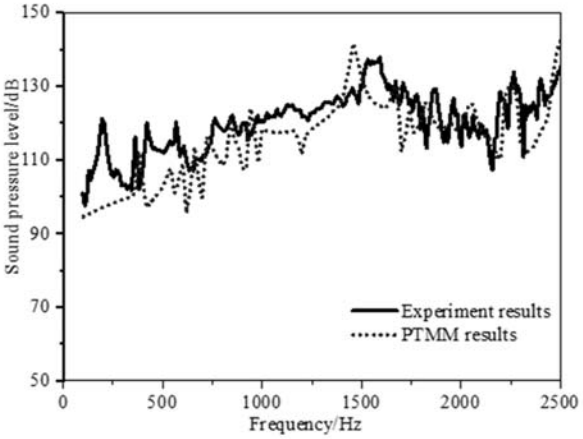

(b)

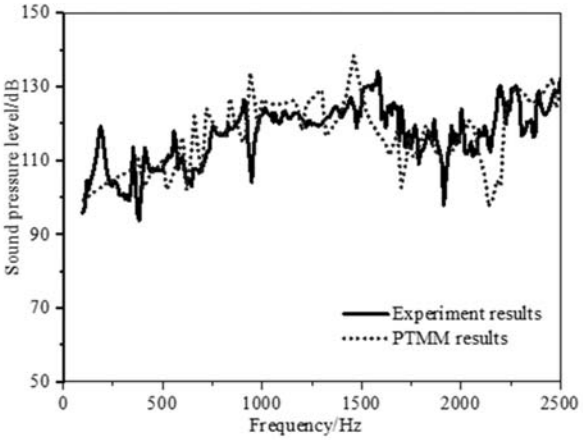

(c)

Fig.13 The underwater sound pressure in force and acoustic excitation case: (a) hydrophone 1, (b) hydrophone 2, (c) hydrophone 3

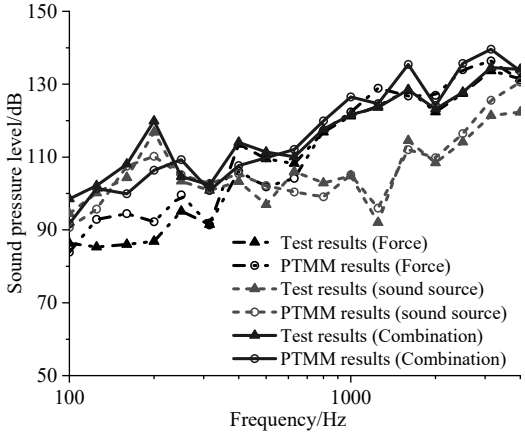

(a)

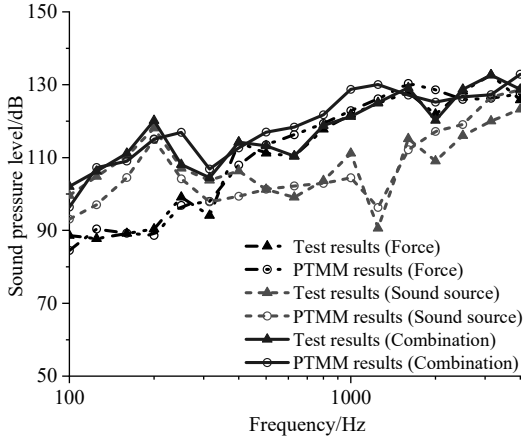

(b)

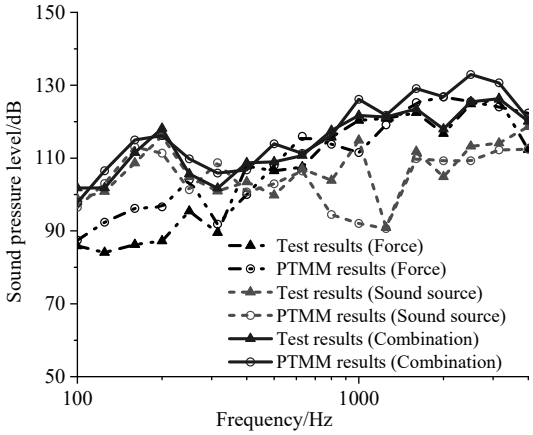

(c)

Fig.14 Underwater sound pressure with fixed frequency under different excitations: (a) hydrophone 1, (b) hydrophone 2, (3) hydrophone 3

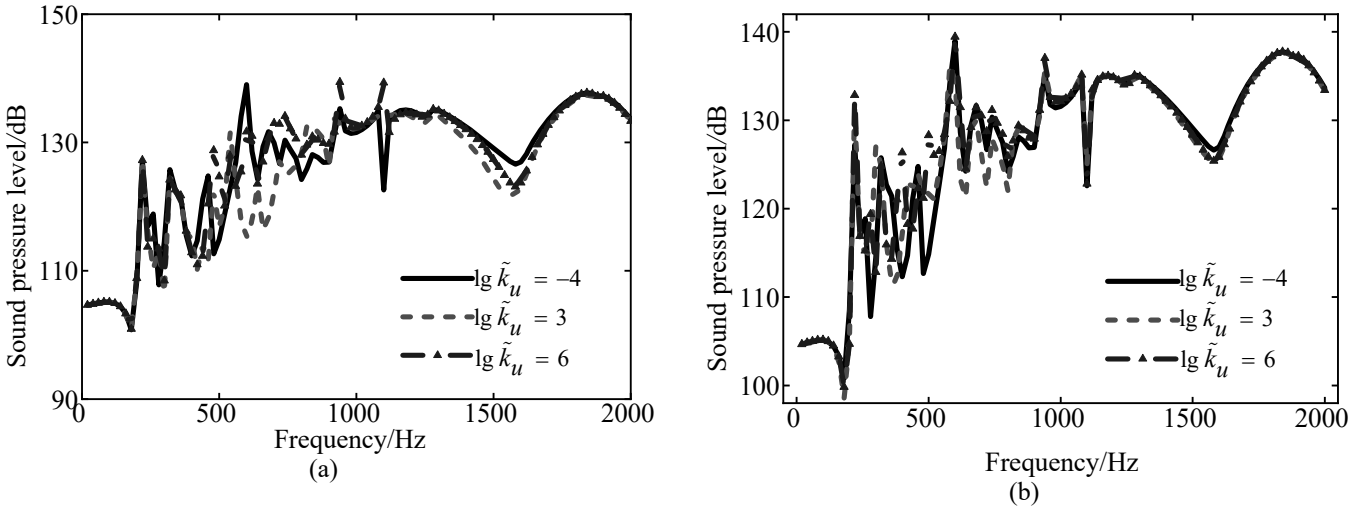

Fig.15 Effect of axial restrains stiffness: (a) inner shell with an elastic boundary; (b) outer shell with an elastic boundary

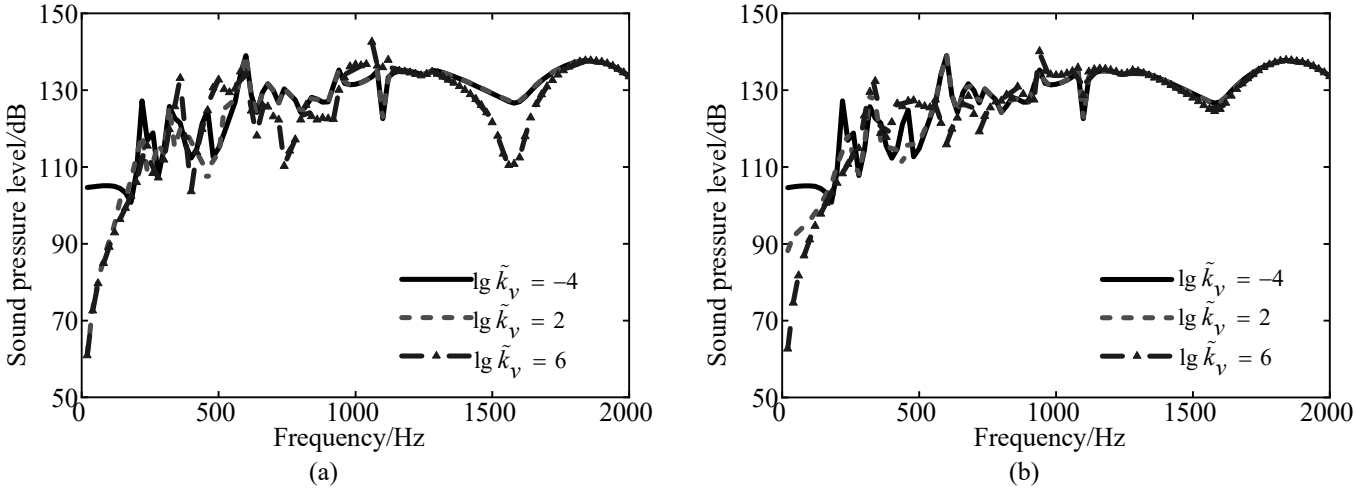

Fig.16 Effect of tangential restrains stiffness: (a) inner shell with an elastic boundary; (b) outer shell with an elastic boundary

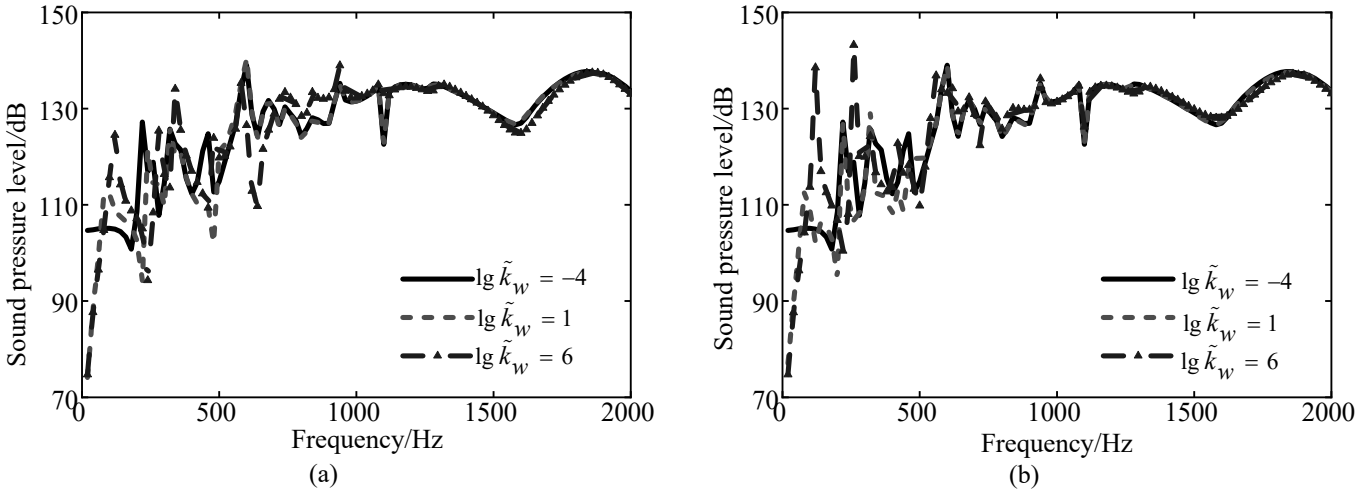

Fig.17 Effect of radial restrains stiffness: (a) inner shell with an elastic boundary; (b) outer shell with an elastic boundary